Sigma Journal of Engineering and Natural Sciences
Web page info: https://sigma.yildiz.edu.tr
DOI: 10.14744/sigma.2025.1921

Research Article

Numerical investigations on the effect of submergence depth and surface wave effect on autonomous underwater vehicle

B. Sairam PRASAD[1], G. Ravikiran SASTRY[1,*]

[1]*Department of Mechanical Engineering, NIT Andhra Pradesh, Tadepalligudem, 534101, India*

ARTICLE INFO

Article history
Received: 08 January 2025
Revised: 13 March 2025
Accepted: 14 July 2025

Keywords:
Autonomous Underwater Vehicle; Computational Fluid Dynamics; Drag; Hydrodynamics; Lift; Stability; Submergence Depth

ABSTRACT

This research conducts a comprehensive numerical investigation into the hydrodynamic behavior of an Autonomous Underwater Vehicle working under the influence of surface waves at different submergence depths (S/D). Results reveal that increasing S/D from 4 to 16 reduces drag and lift coefficients by 10.12% and 20.97%, respectively, due to improved flow symmetry and reduced pressure gradients. The moment coefficient also decreases by 6.23%, enhancing vehicle stability. These findings underscore the critical role of submergence depth in minimizing wave-induced effects, improving efficiency, and optimizing AUV design and operational strategies in dynamic marine environments.

Cite this article as: Prasad BS, Sastry GR. Numerical investigations on the effect of submergence depth and surface wave effect on autonomous underwater vehicle. Sigma J Eng Nat Sci 2026;44(3):1993–2004.

INTRODUCTION

In recent times, it has become evident that Autonomous Underwater Vehicles (AUVs) have grown in popularity and are now considered important components of underwater activities, oceanic research, and even military applications. These vehicles do not require a pilot on board, are equipped with engines, and are capable of self-directed navigation while accomplishing various duties such as surveying the ocean floor, observing the ecosystem, and conducting inspections below the ocean surface [1]. A stylistic and engineering measure known as hydrodynamics is an important aspect of any design, and in this case, the designers of autonomous underwater vehicles may be faced with certain contributions from a variety of operational and environmental forces. One such key contribution is the depth at which an AUV is deployed. This near depth is defined as the AUV Depth of Submergence. This also affects the buoyancy and surrounding water pressure. For instance, if the device is changed in submersed depth, it can make the unit unstable due to other contributing factors such as the variable water pressure, temperature, and density. Therefore, the presence of variable water temperature, pressure, and density at different depths makes the AUV difficult to control, which reinforces the importance of focusing on the relationship between the depth of submergence and the operation performance of the AUV [2]. A concern in shallow depth regions is also that AUVs may be impacted more by the variable wave forces and turbulence's physical impacts. In contrast, at greater depths, the increased water

***Corresponding author.**
*E-mail address: grksastry@nitandhra.ac.in

This paper was recommended for publication in revised form by Editor-in-Chief Ahmet Selim Dalkilic

Published by Yıldız Technical University Press, İstanbul, Turkey

pressure and reduced wave effects can enhance hydrodynamic efficiency but pose challenges related to structural integrity and energy consumption [3].

Ali Nematollahi et al. [4] evaluated the behaviour of an underwater vehicle moving near the free surface by using ANSYS CFX software and reported that there is an increase in hydrodynamic resistance across various speeds operating near the free surface. Tian et al. [5] examined the influence of submersion ratio (h/D) on flow interactions with the free surface and surface waves in the design and operation of autonomous underwater vehicles. The outcomes of the study have provided valuable insights regarding the hydrodynamic performance of AUVs. Jian Cao [6] examined the hydrodynamic behaviour of an open channel's free surface model. Their findings revealed that the free surface does not affect an AUV when its depth is greater than 3.1D, where D is the depth of submergence. Patel [7] reviewed various methods developed over the past decade for calculating unseparated axisymmetric flow over the tail of a body of revolution. It concludes that some computational techniques have now advanced to the point where they can provide quite accurate solutions for these types of flows. O. Saout[8] introduced a theoretical methodology to assess the directional stability of near-surface underwater vehicles. It involves solving coupled sway and yaw motion equations, similar to methods used for surface ships, with stability derivatives obtained through numerical simulations, planar motion mechanism (PMM) tests, and finds that this approach is a valuable tool for determining an underwater vehicle's stability for specific configurations, helping to assess mission viability in advance. Granville, P.S. [9] developed a new empirical relation to determine the position of self-excited transition in low-turbulence flows for calculating the viscous drag on bodies of revolution in axial motion using boundary-layer theory. P. Jagadeesh et al. [10] stated that the k-ε RNG model provides better performance in evaluating the free surface waves effects by comparing with different turbulence models on an axisymmetric underwater body. Nouri [11] focused on optimizing the nose section based on pressure distribution and geometry, emphasizing the pressure drag component. Zhang et al. [12] focused on optimizing hull forms to minimize wave-making resistance, a key application of wave resistance theories. The proposed optimization design method combines Computational Fluid Dynamics (CFD) with the Rankine source method and nonlinear programming (NLP). The results show that the Rankine source method effectively optimizes ship hulls. Miller et al. [13] carried out an experimental study to determine the optimal amplitudes and frequencies for Virtual Planar Motion Mechanism tests of Autonomous Underwater Vehicles and reported that, for typical AUV geometries, non-dimensional frequencies up to 0.5 and non-dimensional amplitudes up to 0.25 are still effective, even considering the influence of fluid memory effects. Salari [14] investigated the free-surface effects of AUVs and found that there is a negligible impact for certain submersion ratios. T. Sarkar et al. [15] studied the influence of various turbulent models on the flow around axisymmetric bodies by using three high-Reynolds-number k-ε turbulence models, like standard, Chen, and Kim-modified, and RNG-derived. The results indicate that the standard model with wall functions predicts flow characteristics as accurately as the other two models.

Amiri et al. [16] investigated the influence of the leeward vortical flow structure on the hydrodynamic behavior of a shallowly submerged UV traveling beneath the free surface at a moderate drift angle. The results show that a significant interaction between the low-pressure region is created by the leeward vortical flow structure and the free surface. Ignacio et al. [17] Conducted an extensive study on the optimal nose profile for deep-water operations, considering velocity and pressure distributions along with overall drag. Kilavuz et al. [18] explored the flow characteristics of an optimized torpedo-like geometry with an elliptical nose, considering angles of attack and submersion ratios. Their study highlighted the influence of jet-like flow and velocity fluctuations on the drag coefficient. Sh. Mansoorzadeh [19] analysed the impact of free surface on the drag and lift coefficients of an AUV. Results indicated that the drag and lift coefficients of the AUV are highly sensitive to changes in submergence depth and speed. Moonesun et al. [20] investigated the impact of surface waves on submarines at various depths to evaluate how depth affects submarine movements using Computational Fluid Dynamics (CFD) tools in Flow-3D, applying Reynolds Averaged Navier-Stokes (RANS) equations and the Volume of Fluid (VOF) method. The findings are aligned with the experimental data. Liu et al. [21] focused on the complex flow physics around underwater vehicles. By using dynamic grid technology, the volume of fluid method, and the finite volume method, the research simulates the flow field around large submerged bodies, particularly their effects on the free surface. The study finds that disturbances on the free surface caused by a moving body are influenced by the body's shape, size, speed, and depth of submergence. Jin Guo et al. [22] examined the hydrodynamic characteristics of a disk-shaped AUV moving near the free water surface and found that changes in flow velocity near the hull, induced by the free surface, are a primary factor influencing the hydrodynamic behaviour. Specifically, these changes were found to increase the resistance on the AUV hull. B.E. Launder [23] addresses the most effective approach in turbulence models that calculate the turbulence kinetic energy and its dissipation rate from transport equations solved alongside the mean flow equations by comparing the nine distinct types of turbulent flow, highlighting its balance of computational efficiency, applicability, and physical realism. Kai Lv et al. [24] investigated the hydrodynamic performance of a vehicle on a water surface. Their studies revealed a maximum reduction in drag of 43% and an improvement in the stability of the vehicle. Foroushani [25] evaluated the hydrodynamic derivatives of the SUBOFF model through steady-state analysis. Ozgoren [26] investigated the performance of an optimized torpedo-like geometry using LES turbulence and VOF multiphase models and found that asymmetrical flow characteristics were observed near the free surface. Le [27] investigated the performance parameters such as drag and lift for a Torpedo-Shaped Underwater Glider corresponding to different velocities and angles of attack. Amory [28] conducted numerical simulations to determine the distribution of velocity and pressure over two different bodies, namely the SEMBIO hull and the MONSUN hull. Takahashi [29] investigated to determine an efficient approach to evaluate the performance characteristics based on the DARPA SUBOFF model, found suitable by comparing it with experimental data. Gupta[30] investigated the effect of step inclination angle (15°, 30°, 45°, 90°) and expansion ratio (1.5 and 2.0) on reattachment length (Lr) behind a backward-facing step. Using ANSYS Fluent and the k-ε turbulence model, it was found that Lr increases with higher step angle and Reynolds number. The results were validated with experimental data, confirming the accuracy of the simulation approach. Rawat [31] examined the influence of axis ratio and shear velocity profiles on drag, pressure distribution, and separation point around a 2D streamlined cylinder at high Reynolds numbers (0.5×10^6 to 3.6×10^6). Results showed that more streamlined cylinders (lower axis ratio) significantly reduced drag up to 60% compared to circular cylinders and delayed flow separation. Shear velocity profiles yielded slightly higher drag than uniform profiles but provided better back pressure recovery. Kukreja et al. [32] analyzed a Busemann-type biplane geometry under supersonic conditions. The optimized biplane design demonstrated a significant reduction in wave drag compared to conventional airfoils. The study highlighted favorable shockwave interactions and suppressed shockwave formation, enhancing aerodynamic performance at high speeds. Kulshreshtha et al. [33] compared the lift and drag coefficients of three NACA airfoils over a wide range of angles of attack (–5° to 20°). Results showed that lift increased with angle of attack until a critical point of 18 to 19°, after which stall occurred. NACA 2415 showed the highest lift but also the highest drag. The study emphasized optimal angle selection for maximizing the lift-to-drag ratio in aerodynamic design. Yuan [34] investigated the flow behaviour and hydrodynamic forces of the vehicle having control fins. Phillips et al. [35] investigated the stability of a torpedo-shaped AUV and found suitable results with the experimental data. This introduction provides how variations in depth influence factors such as drag, lift, and overall vehicle dynamics. Sunil Kumar et al. [36] evaluated the performance of an optimized K-type propeller and reported that aluminum bronze coating achieves a maximum propulsive efficiency of 85%, which is 12% higher compared to conventional rotors, particularly in terms of reducing noise and cavitation.

Zhang et al. [37] developed a numerical model to simulate the water entry of complex curved structures under wave conditions. The findings contribute to a better understanding of wave-induced slamming loads, essential for designing marine structures, ship hulls, and offshore platforms to withstand harsh wave environments. Huang et al. [38] studied by employing the VOF model, Schnerr–Sauer cavitation model, and velocity boundary wave generation method to analyze projectile water entry under Various wave heights, directions, and positions with a water entry angle of 60° and validated through experiments, reported that at 1.3 m wave height, the impact pressure peak rises by 30.9% compared to hydrostatic conditions. The study provides a reference for optimizing projectile water entry under varying wave conditions. Wang et al. [39] developed a 2D model to investigate payload hydrodynamic forces, pressure distributions, and free surface variations during wave entry at different crest or trough positions and sloping directions. The cylinder experiences unequal pressure distributions due to wave particle velocity, together with wave slope variations. The force dynamics become uneven when the entry velocity increases because it creates bigger cavities, which disturb hydrodynamic stability. Cui et al. [40] developed the SPH method to simulate structure-water interaction using open boundary conditions to simulate free slamming of curved wedges and reported that the maximum slamming force in hydrostatic water is proportional to the square of the initial velocity. Convex and reverse curved wedges experience peak vertical slamming loads at different immersion depths due to variations in bottom curvature.

Unlike conventional studies that focus on AUV hydrodynamics at a fixed depth, this work systematically explores how varying submergence depth (S/D) affects hydrodynamic forces and pressure distributions. The study provides quantitative insights into how AUV performance changes with depth, offering optimal operational guidelines for real-world deployment. While many prior studies assume calm water conditions, this research incorporates surface wave interactions, which significantly impact stability, resistance, and maneuverability at shallower depths. The study reveals how wave-induced disturbances alter the pressure and velocity fields, leading to new strategies for wave-adaptive AUV design and control. The work employs advanced CFD simulations with high-resolution turbulence models to capture flow separation, vortex dynamics, and wake structures under varying depth and wave conditions. The use of accurate boundary conditions and wave models enhances the realism of the study, making it more applicable to practical AUV operations. By analyzing pressure distribution, this study provides insights into the optimal submergence depth for minimum drag and maximum efficiency. The findings can guide AUV design improvements, such as hull shaping and control strategies, to enhance underwater endurance and stability. This research presents a novel numerical investigation that bridges theoretical hydrodynamics and practical AUV operations by systematically evaluating submergence depth and surface wave effects. The findings contribute to efficient AUV design, enhanced operational strategies, and improved hydrodynamic performance in dynamic underwater environments.

The rest of the paper is organized as follows: in Section 2, the method and methodology, along with the governing equation, computational domain, mesh generation, boundary conditions, and numerical validation, will be presented. In Section 3, the outcomes of the work will be presented.

MATERIALS AND METHODS

AUV Structure

The AUV considered in this study is a four-numbered NACA 0012 profile having a mass of 77.64 kg. There are three main hull forms used for AUVs: Myring's Profile, Jackson's Profile, and Gertler's Series 58 Profile. Although the equations for these profiles differ, they essentially represent similar shapes with minor variations [41]. Figure 1 represents the shape of the AUV. The AUV geometry is typically divided into three sections: the nose, the body, and the tail, all designed using Myring's equations[42]. To design the nose and tail shapes, the following equations are employed:

$$R_1(x_1) = \frac{1}{2}\, D \left[1 - \left(\frac{x_1 - a}{a}\right)^2\right]^{\frac{1}{n}} \tag{1}$$

$$R_2(x_2) = \frac{1}{2} D - \left[\frac{3D}{2C^2} - \frac{\tan\theta}{C}\right] x_2^2 + \left[\frac{D}{C^3} - \frac{\tan\theta}{C^2}\right] x_2^3 \tag{2}$$

Table 1. Dimensional parameters of AUV

Description	Value
Nose Length (a)	0.15 m
Hull Length (b)	1.25625 m
Tail Length (c)	0.41875 m
Maximum diameter (D)	0.25 m
Tail half angle (θ)	25°
Myring body parameter (n)	2
Length of AUV (L)	1.825 m

where D represents the maximum diameter of the model; a represents the length of the nose; x_1 represents the location of the nose tip; c represents the length of the tail; θ represents the tail half angle in degrees; n represents the Myring body parameter; x_2 represents the location of the tail tip; L represents the length of the AUV. The dimensions of the profile are illustrated in Table 1. The control surface is NACA 0012, having a mean span and chord length of 0.060525 m and 0.25 m, respectively. The reason behind choosing the selected dimensional parameters is due to their slenderness ratio (L/D ≈ 7.3), which falls within the typical range of streamlined AUV designs, ensuring low drag and efficient hydrodynamic performance. The NACA 0012 symmetric airfoil with a maximum thickness of 12% of the chord length is commonly used in AUV control surfaces due to its low drag characteristics and stable hydrodynamic response. A chord length of 250 mm is appropriate for maintaining effective control forces while minimizing flow separation in underwater conditions. The thin, symmetric profile ensures predictable lift and moment characteristics, reducing unwanted pitching and yawing tendencies.

To clearly define the AUV exposed to wave current, Figure 2 illustrates the dimensional aspects of the wave, including wavelength (λ), wave height (H), submerged depth (S), and water depth (h). Employing nonlinear wave theory, the waves are scaled using the nondimensional parameter steepness (H/λ). The corresponding value of wave steepness for a wave height of 0.30 m and a wave length of 2 m is 0.15. Waves with a relative depth (h/λ) greater than 0.5 are classified as deep-water waves[43]. The inflow velocity, based on the length-scaled Reynolds number, is 2.73 x 10^6.

The non-dimensional hydrodynamic coefficients used to describe the forces of the AUV are,

$$C_d = \frac{F_x}{0.5\rho L^2 u^2} \tag{3}$$

$$C_l = \frac{F_y}{0.5\rho L^2 u^2} \tag{4}$$

$$C_m = \frac{F_z}{0.5\rho u^2 L^3} \tag{5}$$

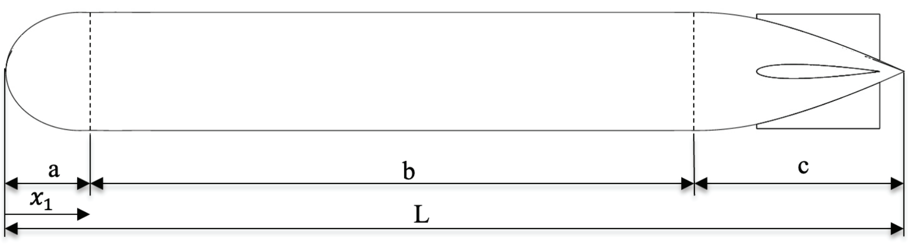

Figure 1. Shape of the AUV.

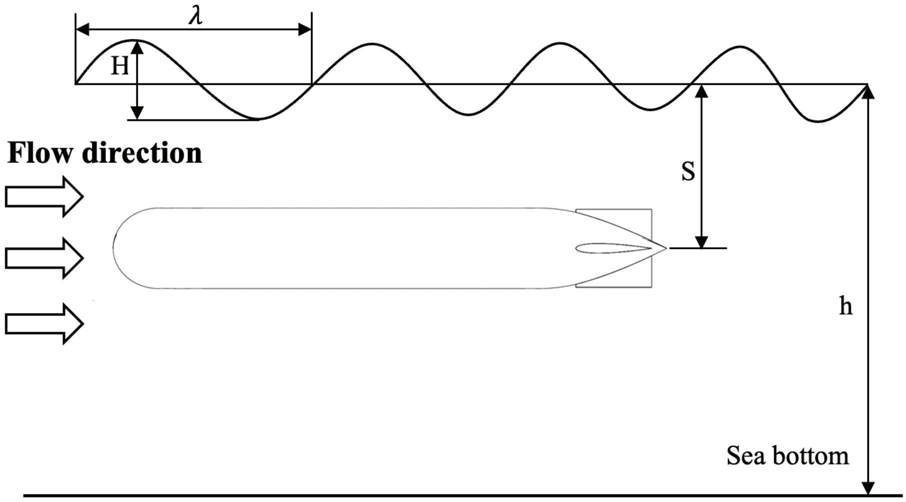

Figure 2. Illustration of an AUV exposed to waves and current.

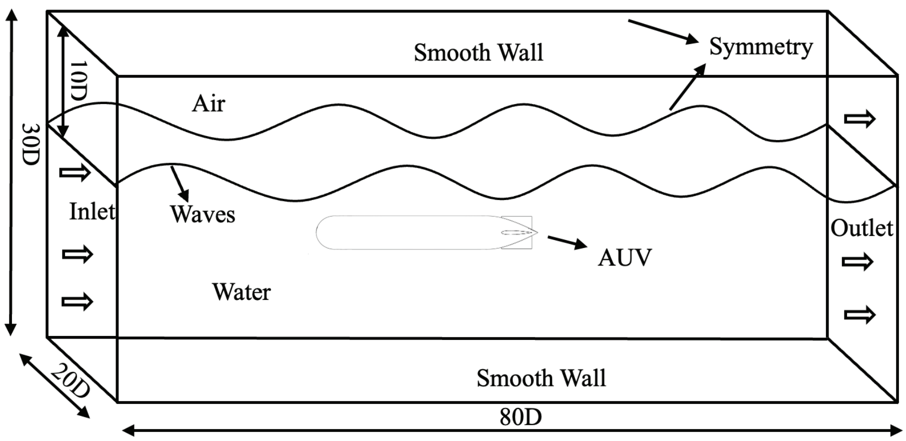

Figure 3. Schematic representation of computational domain.

Here, C_d, is the drag coefficient, C_l, is the lift coefficient, and C_m is the moment coefficient of the AUV. F_x, F_y, and F_z represent the drag force, lift force, and moment, respectively. ρ is the water density. u is the inflow velocity. This study aims to investigate the hydrodynamic characteristics of the AUV, specifically focusing on two crucial factors, namely depth of submergence and the impact of surface waves.

GOVERNING EQUATIONS

Considering the influence of gravity, a series of transient three-dimensional Computational Fluid Dynamics (CFD) simulations were performed to evaluate the performance of the AUV. The ANSYS Fluent was used to solve the Reynolds-averaged Navier-Stokes (RANS) equations with a SIMPLE pressure-velocity coupling scheme. The governing equations include the continuity equation and the momentum equation, which are given below.

$$\frac{\partial \rho}{\partial t} + \frac{\partial \rho \overline{v_i}}{\partial x_i} = 0 \tag{6}$$

$$\frac{\partial}{\partial t}(\rho \overline{v}_i) + \frac{\partial}{\partial x_i}(\rho \overline{v_i}\overline{v_j}) = -\frac{\partial p}{\partial x_i} + \frac{\partial}{\partial x_j}\left[\mu\left(\frac{\partial \overline{v_i}}{\partial x_j} + \frac{\partial v_j}{\partial x_i} - \frac{2}{3}\delta_{ij}\frac{\partial v_l}{\partial x_l}\right)\right] - \frac{\partial}{\partial x_j}\left(\rho \overline{v'_i v'_j}\right) + F_i \tag{7}$$

In the equations v_i represents the velocity components, p denotes the total pressure, Fi represents the external body force components, and μ denotes the dynamic viscosity. The velocity v_i is the combination of the time-averaged value $\overline{v_i}$ and the fluctuation ϑ_i'.

The Shear Stress Transport (SST) k-ω turbulence model was chosen to handle the turbulence terms in the RANS equations. The reason behind choosing the shear stress transport omega turbulence model is its ability to accurately predict turbulent flows near walls and in boundary layers. It addresses the deficiencies of some other models in capturing the near-wall behavior, making it particularly suitable for simulations involving complex geometries or flows with significant boundary layer effects. The model computes the turbulent kinetic energy, k, and the specific dissipation rate, ω, using the following equations:

$$\frac{\partial}{\partial t}(\rho k)+\frac{\partial}{\partial x_i}(\rho k v_i)=\frac{\partial}{\partial x_j}\left(\tau_k \frac{\partial k}{\partial x_j}\right)+G_k-Y_k+S_k \tag{8}$$

$$\frac{\partial}{\partial t}(\rho \omega)+\frac{\partial}{\partial x_j}(\rho \omega v_j)=\frac{\partial}{\partial x_j}\left(\tau_\omega \frac{\partial k}{\partial x_j}\right)+G_\omega-Y_\omega+S_\omega \tag{9}$$

where G_k and G_ω represent the generation of k and ω resulting from turbulent mean-velocity gradients, respectively, Γ_k and Γ_ω signify effective diffusivity, while Y_k and Y_ω represent the dissipation of k and ω due to turbulence, D_ω represents the cross-diffusion term, and S_k and S_ω are user-defined source terms.

The Volume of Fluid (VOF) model[44] is used to predict fluid behaviour, effectively representing the interface between the air and water surfaces caused by wave propagation. This method relies on the concept of air-water mixture velocity, which involves tracking the volume fraction of each fluid phase within the computational domain.

$$v_i = \sigma v_i^a + (1-\sigma) v_i^w \tag{10}$$

where σ represents the volume, fraction equals 1 when fully occupied by air, v_i^a denotes the velocity for the phase of air, and v_i^w denotes the velocity for the phase of water.

In the case of deep-water waves, nonlinear wave theory [45] is generally used. It refers to a generation of waves whose behavior deviates significantly from linear wave theory. In linear wave theory, waves are assumed to interact weakly with each other, whereas in nonlinear wave generation, the interactions between waves become significant, leading to phenomena such as wave steepening, wave breaking, and the generation of higher harmonics. In this study, third-order Stokes wave theory is utilized. The reason behind choosing third-order Stokes wave theory is due to its accuracy in deep water depths, wave steepening, and nonlinear effects. The expression for the wave profile is

$$\eta(x,t)=a\cos(Kx-\omega_0 t)+\tfrac{1}{2}Ka^2\cos(2Kx-2\omega_0 t) + \tfrac{3}{8}Ka^3\cos(3Kx-3\omega_0 t) \tag{11}$$

where η denotes the surface elevation of the wave, a represents the wave amplitude, and K represents the wave number, ω_0 signifies the wave frequency, x denotes the horizontal distance, and t represents the time.

In the case of deep-water waves, the wave number K and wave frequency ω are related as

$$\omega^2 = gK \tag{12}$$

where g is the acceleration due to gravity.

Mesh Generation and Validation

Figure 3 represents the computational domain with boundary conditions. A high-quality mesh, as illustrated in Figure 4, was generated using ANSYS Fluent to estimate the uncertainties on the hydrodynamic performance of the AUV. Numerical uncertainties are estimated by multiplying the numerical error by a safety factor. The numerical error consists of three parts, i.e., round-off error, iterative error, and discretization error [46,47]. Round-off error is minimized due to the use of double precision during setup conditions. The iterative error is the difference between the current numerical solution and the theoretically converged solution obtained after a large number of iterations. Discretization error is the difference between the exact solution of the continuous problem and the solution of the discretized problem. Seven different mesh grids were studied to evaluate the grid independence, and observed that more than 5.8 million elements have a skewness error percentage less than 1.5%, as shown in Figure 5. Elements beyond 5.8 million are independent of changes in solution with a y+ value of 30. So, 5.8 million elements are considered in this study. The value of skewness considered in this study is 0.78. The simulations were performed at a

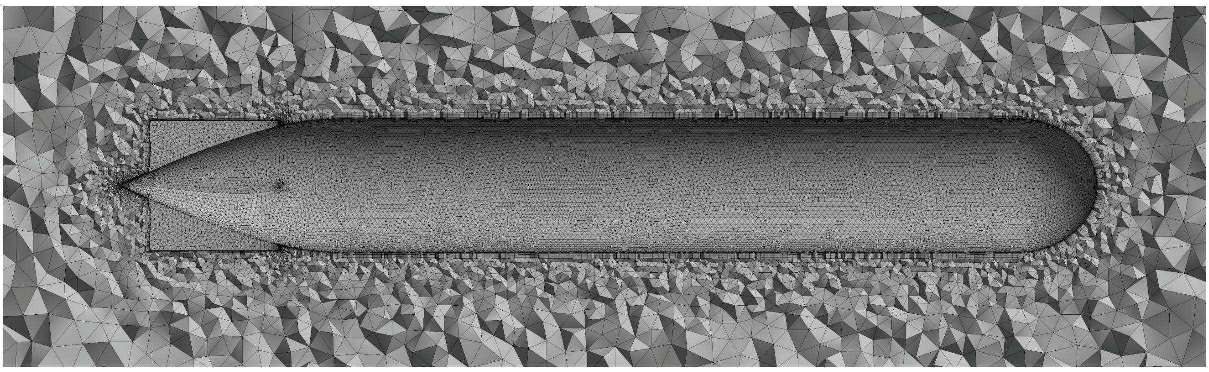

Figure 4. Mesh generation.

submergence depth of 1m, with a velocity of 1 m/s under no-wave conditions. The AUV is positioned one-third of the way from the left boundary and submerged at a depth of 4D below the free surface. Boundary conditions include an open channel wave boundary with uniform velocity at the inlet, a pressure outlet at the outlet, no-slip wall conditions on the AUV surfaces, smooth wall conditions at the top and bottom boundaries, and symmetry conditions on the domain's sides. Wave propagation is simulated by applying an open channel wave boundary on the left side, using a shallow/intermediate wave as the boundary condition. Both the wave heading angle and phase difference are set to zero to ensure consistent alignment of wave propagation.

Validation is performed by comparing the CFD results with wave elevation data calculated using Stokes wave theory. The accuracy of the numerical method is evaluated based on its ability to accurately predict both the hydrodynamic coefficients under calm conditions and the shape of the wave. Figure 6 represents the validation of drag coefficients corresponding to different velocities. It's important to note that the drag coefficients were calculated relative to the length of the AUV. It is observed that the values are in good agreement with the data provided by Ali Nematollahi et al. [4], with a minimum percentage of 5.11% obtained for a Reynolds number of 3.645 x 10^5 and a maximum percentage of 13.04% obtained, corresponding to a Reynolds number of 1.0 x 10^5. Figure 7 presents a comparison of wave elevation over time, showing a strong correlation between the CFD and analytical results. However, the CFD method predicts a slightly lower wave height compared to the analytical solution due to the physical properties of water, like viscosity. A convergence criterion of 10^{-3} was applied with a time step size of 0.002 based on stability analysis with the CFL criterion.

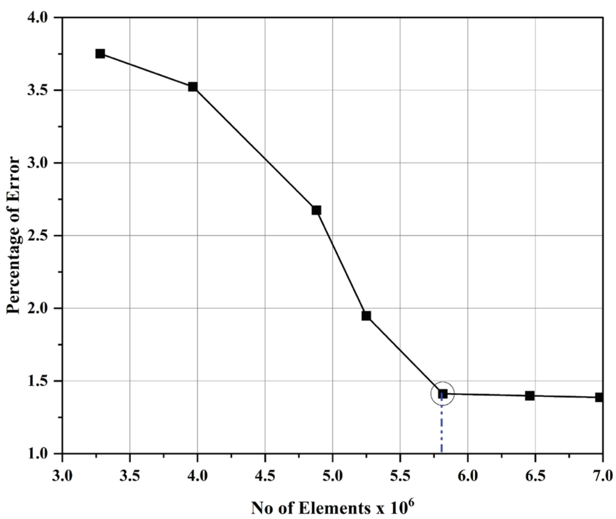

Figure 5. Grid independence test.

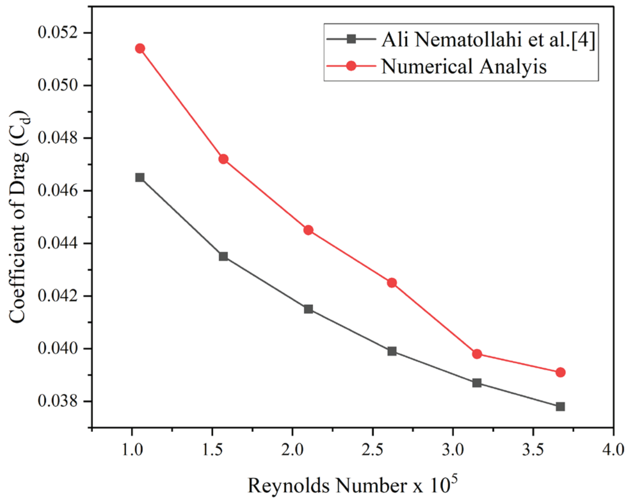

Figure 6. Validation of drag coefficient.

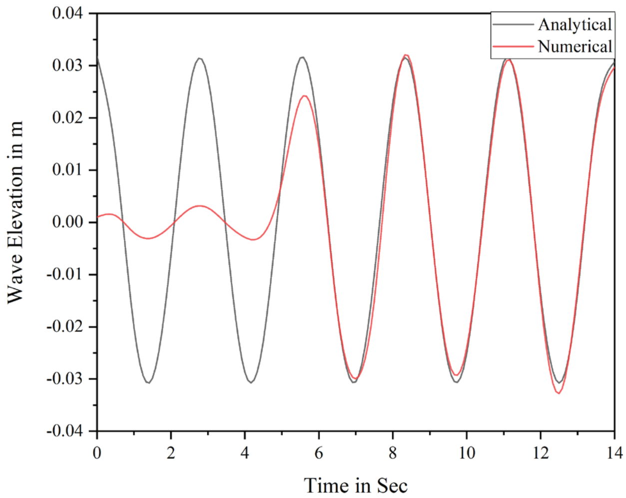

Figure 7. Validation of the wave.

RESULTS AND DISCUSSION

Influence of Submerged Depth on Hydrodynamic Parameters

The submergence depth significantly affects the hydrodynamic forces acting on submerged objects, such as drag, lift, and moment. The drag coefficient decreases steadily with increasing submergence depth. At S/D = 4, the drag coefficient is at its maximum, but as the AUV is submerged deeper, the coefficient of drag decreases from 0.002285 to 0.002054. This trend suggests that deeper submergence results in lower resistance forces acting on the AUV, likely due to lower interaction with the surrounding fluid. The lift coefficient shows a monotonic behaviour with submergence depth, decreasing from 0.144055 to 0.113835,

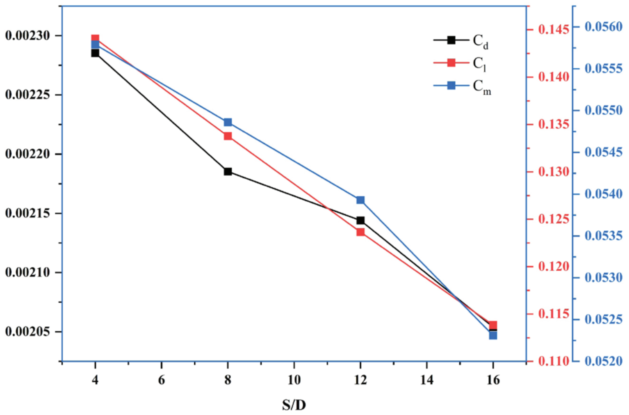

Figure 8. Effect of hydrodynamic parameters on different depths of submergence.

indicating that the upward pressure difference across the AUV decreases. The moment coefficient follows a clear decreasing trend with submergence depth. This suggests that the coefficient of moment decreases due to a more symmetric distribution of pressure and a lesser change in the shift of the centre of pressure along the AUV's body, as shown in Figure 8.

At a submergence depth of 1m, the hydrodynamic coefficients are at their highest. The proximity to the wave crest results in strong wave-induced forces acting on submerged objects. The lift experienced by submerged objects is also significant at this depth due to the high-pressure differentials and force magnitudes. At S/D = 8, wave energy dispersion starts to take place in such a manner that there are lower force magnitudes on the submerged objects due to the dissipation of energy. Interaction with the wave becomes more stable as the forces witness a reduction in fluctuations. At S/D = 12, the hydrodynamic parameters have even lower drag and lift. The wave has a minimal effect on the submerged objects in this associated condition. With this association, the moments experienced by the objects also get smaller with the further reduction of pressure differentials. However, the forces demonstrate consistent and moderate fluctuations. At a depth of submergence of S/D = 16, the representation of drag and lift can almost be disregarded. Wave energy has dissipated greatly, and the forces are weak. The representation of moments remains at insignificant values because of the low-pressure difference. Because of this, the forces are very consistent as the influence of the wave is not prominent.

Influence of Submerged Depth on Velocity Contours

As the submergence depth (S/D) ratio increases, the contours display lower concentrations and disruptions of the velocity, displaying a direct dependency on the disruption created by the flow around the body. It is indicative that at lower S/D values, S/D=4, the resistance factors around the submerged body exhibit major disturbances because of surface factors in the fluid domain. These disturbances create localized regions of higher velocity gradients, which contribute to increased drag and lift forces, as evidenced by the relatively higher Cd = 0.002285 and Cl = 0.144055. The non-uniformity in velocity fields at shallow depths can lead to unsteady forces and reduced stability. As the submerged depth increases, S/D=8 and S/D=12, the velocity contours become more symmetrical, with smoother flow patterns around the body. This transition reduces the velocity gradients near the surface and minimizes flow separation. Consequently, both the drag coefficient (Cd) and lift coefficient (Cl) decrease, indicating improved hydrodynamic efficiency and stability. At greater depths, S/D=16, the velocity contours show further uniformity, with fewer disturbances in the flow field. The steep velocity gradients observed at shallower depths diminish, and the flow stabilizes around the body. This leads to the lowest drag coefficient Cd = 0.002054 and lift coefficient Cl = 0.113835 in the dataset. Additionally, the reduced moment coefficient Cm = 0.05231 reflects the reduction of pitching or yawing tendencies, contributing to more stable operation. At S/D = 4, the separation region behind the AUV is relatively larger, indicating strong flow detachment due to the proximity to the free surface. As S/D increases, the separation region gradually reduces, suggesting a smoother flow transition with less disturbance from surface effects. At S/D = 16, the separation region is minimal, implying better hydrodynamic stability at deeper submergence. The boundary layer appears thicker at lower submergence depths (S/D = 4, 8) due to increased shear stress and surface interactions. As the submergence depth increases, the boundary layer thickness decreases, showing a more stable and uniform velocity distribution. At higher S/D values (12 and 16), the boundary layer is well-developed and thinner, indicating reduced wall effects and smoother flow. Figure 9 represents the velocity contours corresponding to different depths of submergence. Overall, the deeper the body is submerged, the simpler and more uniform the velocity field becomes, leading to reduced drag, lift, and moments. These changes enhance energy efficiency, stability, and performance, making deeper submergence an advantageous condition for applications requiring precise and stable trajectories, such as underwater vehicles.

Influence of Submerged Depth on Pressure Contours

The pressure contours exhibit distinct variations as the submerged depth ratio increases, as illustrated in Figure 10. These changes in the intensity and distribution of pressure fields are directly linked to the hydrodynamic performance of the submerged body. At a submergence depth of S/D=4, the pressure contours are relatively symmetrical throughout the AUV. This uniformity demonstrates that the fluid interaction is balanced, which does not permit excessive induced pressure to act. At this depth, the symmetric pressure field is at its buoyancy coefficient Cl = 0.144055, and the capacity at which drag

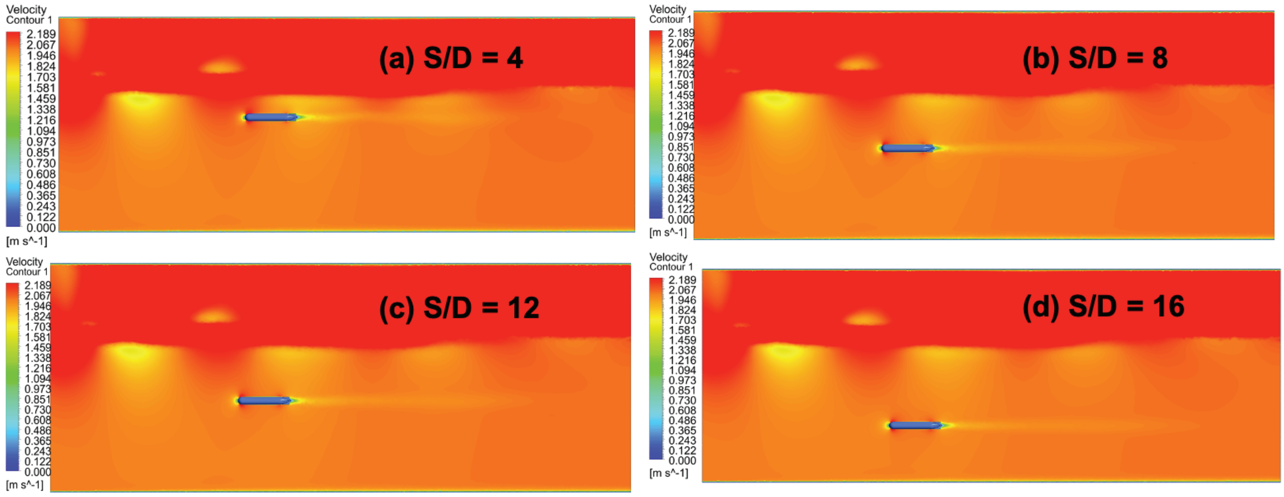

Figure 9. Velocity contours at different depths of submergence ratios at t = 4.8 sec.

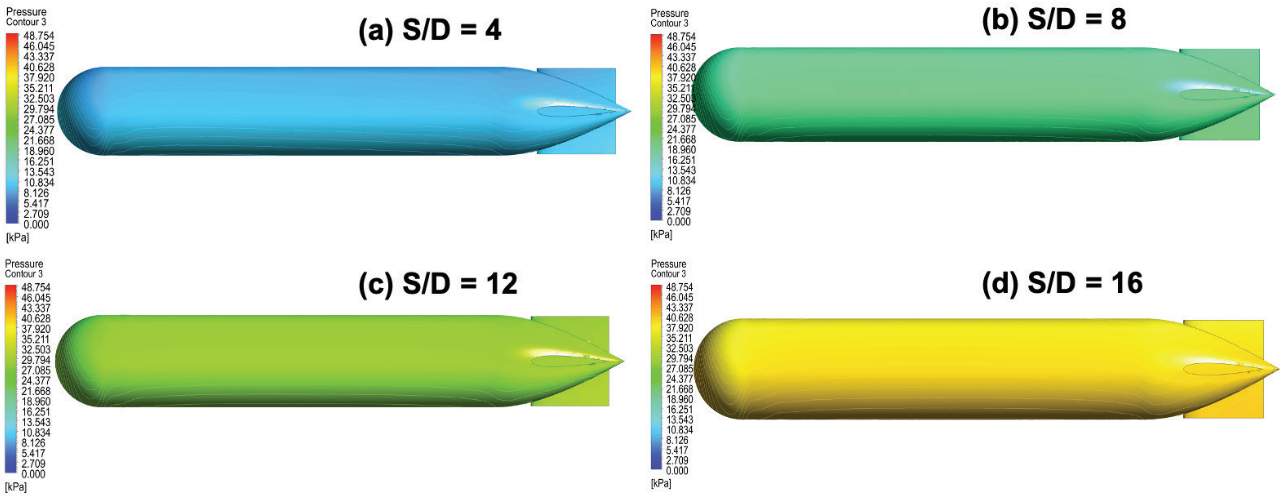

Figure 10. Pressure contours over the AUV at different depths of submergence ratios at t = 4.8s.

can be sustained is moderate Cd = 0.002285. This signifies that the submerged body is in stable operation with an average amount of hydrodynamic forces. Such a balance is conducive to propulsive efficiency as well as for constant trajectories. When the submerged depth is increased to S/D=8, the pressure contours appear to have a more rapid change over the hull surface of the AUV. High-pressure regions appear to be more pronounced towards the bow of the body, while the low-pressure areas form around the stern. This pressure gradient reduces the drag such that Cd = 0.002185 and slightly lowers the lift, Cl = 0.133786, implying that the resistance forces have started building up. Higher resistance forces may call for additional power to be used when in motion, thus affecting the level of operational efficiency. When at a submerged depth of S/D=12, the pressure field shows further stabilization. The pressure variations along the hull are more consistent, and no significant asymmetry is visible. The influence of surface-induced disturbances becomes minimal, and the pressure gradually transitions from high at the stagnation region to low towards the tail, causing further reduction of the lift Cl = 0.123649 and moment coefficients Cm = 0.05393, indicating a shift toward improved stability. At S/D=16, a stable flow regime with a minimum amount of drag Cd = 0.002054, lift force Cl = 0.113835, and moment Cm = 0.05231 is observed. These variations are very important in the design of submerged vehicles and structures like underwater vehicles. At S/D = 4, the high-pressure region at the front of the AUV is more pronounced, and a strong low-pressure region is observed at the stern, indicating early flow separation. As S/D increases, the low-pressure region at the rear becomes less intense, suggesting delayed or reduced separation. At S/D = 16, the pressure distribution is more uniform, indicating a more streamlined flow and minimal separation effects. For S/D = 4, the stern experiences a significantly low-pressure region, indicating an increase in flow detachment. At S/D = 16, the recirculation zone is significantly reduced, leading to better pressure recovery and lower drag. At lower S/D values 4 and 8, the boundary layer appears thicker, indicating higher shear stress and interaction with the free surface. As the AUV submerges deeper, S/D = 12 and 16, the boundary layer becomes thinner and more stable, reducing overall hydrodynamic resistance. The pressure gradient along the hull stabilizes at higher S/D values, which contributes to smoother flow development. Shallow submergence causes stronger separation and thicker boundary layers, increasing drag. Deeper submergence (high S/D) results in smoother flow and thinner boundary layers, leading to improved hydrodynamic performance.

CONCLUSION

It is evident that the drag characteristics, namely, the coefficient of drag, decrease by about 10.12% with an increase in depth of submergence (S/D). This trend demonstrates that as the vehicle is under more depth, the resistive forces encountered are likely reduced due to the fluid's better streamline surrounding the Autonomous Underwater vehicle. There is a monotonic behaviour for the lift coefficient that is similar when submergence depth changes for that of the drag coefficient. This is due to the symmetric distribution of flow regimes and pressure around the Autonomous Underwater vehicle as it submerges deeper, thereby lowering the maximum lift by about 20.97%. The moment coefficient significantly decreases by about 6.23% with depth. This suggests a reduction in pitching or yawing tendency and better stability of the vehicle. At shallow depths, the interaction of autonomous underwater vehicles with surface waves introduces significant changes in pressure and velocity gradients. This led to higher drag, lift, and moment forces, making it challenging to achieve stable operation. As the Autonomous Underwater Vehicle submerges deeper, the influence of surface waves diminishes, and the hydrodynamic forces stabilize. Hull shaping can be optimized to enhance streamlined flow and further reduce drag. This highlights the importance of operating at sufficient depths to avoid wave-induced instability and energy inefficiency. In future work, a detailed study on varying wave steepness, heights, irregular waves, and cavitation phenomena can be conducted to analyse their impact on the performance of the AUV. The present study utilizes velocity conditions that are less likely to induce cavitation; however, future investigations can focus on higher velocity regimes and varying operational conditions to assess cavitation formation and its effects on efficiency.

NOMENCLATURE

a	Length of the nose
A	is the wave amplitude
b	Length of the middle section
c	Length of the tail
D	Maximum diameter of AUV
D_ω	represents the cross-diffusion term
Fi	External body force components
Gk and Gω	represent the generation of k and ω from turbulent mean-velocity gradients.
g	Acceleration due to gravity
H	Wave height
k	Turbulent kinetic energy
K	represents the wave number
L	Length of the AUV
n	Myring body parameter
p	Total pressure
S	Submerged depth
Sk and S_ω	are user-defined source terms
t	Time
v	Velocity of AUV
x_1	Location of the nose tip
x_2	Location of the tail tip
θ	Tail half angle in degrees
ρ	Fluid density
μ	Dynamic viscosity of the fluid
ω	Specific dissipation rate
ω_0	signifies the wave frequency
x	denotes the horizontal distance
. σ	represents the volume fraction.
η	Represents the surface elevation of the wave
θ	Angle at the tail tip
λ	Wavelength
CFL	Courant-Friedrichs-Lewy Condition (Courant Number).

AUTHOR CONTRIBUTIONS

Conceptualization, data collection, and writing initial draft: B Sairam Prasad; supervision: G Ravi Kiran Sastry; All authors reviewed the manuscript.

DATA AVAILABILITY STATEMENT

The authors confirm that the data that supports the findings of this study are available within the article. Raw data that support the finding of this study are available from the corresponding author, upon reasonable request.

CONFLICT OF INTEREST

The author declared no potential conflicts of interest with respect to the research, authorship, and/or publication of this article.

ETHICS

There are no ethical issues with the publication of this manuscript.

STATEMENT ON THE USE OF ARTIFICIAL INTELLIGENCE

Artificial intelligence was not used in the preparation of the article.

REFERENCES

[1] Sahoo A, Dwivedy SK, Robi PS. Advancements in the field of autonomous underwater vehicle. Ocean Eng 2019;181:145–160. [CrossRef]

[2] Yoerger DR, Jakuba M, Bradley AM, Bingham B. Techniques for deep sea near bottom survey using an autonomous underwater vehicle. Int J Rob Res 2007;26:41–54. [CrossRef]

[3] Mitra A, Panda JP, Warrior HV. The effects of free stream turbulence on the hydrodynamic characteristics of an AUV hull form. Ocean Eng 2019;174:148–158. [CrossRef]

[4] Nematollahi A, Dadvand A, Dawoodian M. An axisymmetric underwater vehicle-free surface interaction: A numerical study. Ocean Eng 2015;96:205–214. [CrossRef]

[5] Tian W, Song B, Ding H. Numerical research on the influence of surface waves on the hydrodynamic performance of an AUV. Ocean Eng 2019;183:40–56. [CrossRef]

[6] Cao J, Zhang C, Wu H, Xu L, Liu H. Research on the hydrodynamic performance of AUVs in small size open channel area. Ocean Eng 2023;288:116190. [CrossRef]

[7] Patel VC, Chen HC. Flow over tail and in wake of axisymmetric bodies: Review of the state of the art. J Ship Res 1986;30:201–214. [CrossRef]

[8] Saout O, Ananthakrishnan P. Hydrodynamic and dynamic analysis to determine the directional stability of an underwater vehicle near a free surface. Appl Ocean Res 2011;33:158–167. [CrossRef]

[9] Granville PS. The calculation of the viscous drag of bodies of revolution. Report 849. Washington, DC: David Taylor Model Basin; 1953.

[10] Jagadeesh P, Murali K, Idichandy VG. Experimental investigation of hydrodynamic force coefficients over AUV hull form. Ocean Eng 2009;36:113–118. [CrossRef]

[11] Mohammad Nouri N, Mohammadi S. Numerical investigation of the effects of camber ratio on the hydrodynamic performance of a marine propeller. Ocean Eng 2018;148:632–636. [CrossRef]

[12] Zhang B, Ma K, Ji Z. The optimization of the hull form with the minimum wave making resistance based on Rankine source method. J Hydrodyn 2009;21:277–284. [CrossRef]

[13] Miller LM, Krauss S, Brizzolara S, Gilbert C, Stilwell D. Effect of amplitudes and frequencies on virtual planar motion mechanism of AUVs: Part II 3DOF implementation, comparison with RANSE and field trials. Ocean Eng 2023;289:116242. [CrossRef]

[14] Salari M, Rava A. Numerical investigation of hydrodynamic flow over an AUV moving in the water-surface vicinity considering the laminar-turbulent transition. J Mar Sci Appl 2017;16:298–304. [CrossRef]

[15] Sarkar T, Sayer PG, Fraser SM. Flow simulation past axisymmetric bodies using four different turbulence models. Appl Math Model 1997;21:783–792. [CrossRef]

[16] Amiri MM, Sphaier SH, Vitola MA, Esperança PT. URANS investigation of the interaction between the free surface and a shallowly submerged underwater vehicle at steady drift. Appl Ocean Res 2019;84:192–205. [CrossRef]

[17] Ignacio LC, Victor RR, Francisco DRR, Pascoal A. Optimized design of an autonomous underwater vehicle, for exploration in the Caribbean Sea. Ocean Eng 2019;187:106184. [CrossRef]

[18] Sarigiguzel F, Ozgoren M, Koca K, Sahin B, Akilli H. Experimental investigation of free-surface effects on flow characteristics of a torpedo-like geometry having a cambered nose. Ocean Eng 2022;253:111174. [CrossRef]

[19] Mansoorzadeh S, Javanmard E. An investigation of free surface effects on drag and lift coefficients of an autonomous underwater vehicle (AUV) using computational and experimental fluid dynamics methods. J Fluids Struct 2014;51:161–171. [CrossRef]

[20] Moonesun M, Korol Y, Yuhina D, Dalir A, Atyfi A, Yakovlev A. Effective depth of regular wave on submerged submarine. Indian J Geo-Mar Sci 2019;48:1476–1484.

[21] Liu TL, Guo ZM. Analysis of wave spectrum for submerged bodies moving near the free surface. Ocean Eng 2013;58:239–251. [CrossRef]

[22] Guo J, Zhang Y, Wang Y, Chen Y, Tang Y, Zhang L. Numerical research on hydrodynamic characteristics of the disk-shaped autonomous underwater vehicle near free surface. Ocean Eng 2023;288:116175. [CrossRef]

[23] Launder BE, Spalding DB. The numerical computation of turbulent flows. Comput Methods Appl Mech Eng 1974;3(2):269–289. [CrossRef]

[24] Lv K, Liu H, Gu H, Wang X, Ji X. Hydrodynamic investigations of a cross-domain vehicle with the capability of high-speed cruising on water surface. Ocean Eng 2023;280:114688. [CrossRef]

[25] Foroushani JA, Sabzpooshani M. Determination of hydrodynamic derivatives of an ocean vehicle using CFD analyses of synthetic standard dynamic tests. Appl Ocean Res 2021;108:102539. [CrossRef]

[26] Özgören M, Koca K, Sarigüzel F, Şahin B, Akilli H. Analysis of attack angle effect on flow characteristics around torpedo-like geometry placed near the free-surface via CFD. Politek Derg 2021;24:1579–1592. [CrossRef]
[27] Le TL, Hong DT. Computational fluid dynamics study of the hydrodynamic characteristics of a torpedo-shaped underwater glider. Fluids 2021;6:252. [CrossRef]
[28] Amory A, Maehle E. Modelling and CFD simulation of a micro autonomous underwater vehicle SEMBIO. In: OCEANS 2018 MTS/IEEE Charleston; 2018 Oct 22–25; Charleston, SC, USA. IEEE; 2019. p. 1–6. [CrossRef]
[29] Takahashi K, Sahoo PK. Fundamental CFD study on the hydrodynamic performance of the DARPA SUBOFF submarine. In: Proceedings of the ASME 2019 38th International Conference on Ocean, Offshore and Arctic Engineering (OMAE2019); 2019 Jun 9–14; Glasgow, Scotland, UK. ASME; 2019. [CrossRef]
[30] Gupta SK, Kukreja N. CFD analysis of flow over backward facing step at different inclination angle. Int J Adv Sci Technol 2020;29(3):4696–4701.
[31] Rawat MK, Gupta SK. Effect of plain shear velocity profile over a streamline cylinder. Int J Eng Adv Technol 2019;8:396–399.
[32] Kukreja N, Gupta SK, Rawat MK. Performance analysis on biplane structure at different Mach numbers. Int J Sci Technol Res 2020;9:3541–3546.
[33] Kulshreshtha A, Gupta SK, Singhal P. FEM/CFD analysis of wings at different angle of attack. Mater Today Proc 2019;26(P2):1638–1643. [CrossRef]
[34] Yuan X, Xing T. Hydrodynamic characteristics of a supercavitating vehicle's aft body. Ocean Eng 2016;114:37–46. [CrossRef]
[35] Phillips A, Furlong M, Turnock SR. The use of computational fluid dynamics to determine the dynamic stability of an autonomous underwater vehicle. Proc Inst Mech Eng M J Eng Marit Environ 2016;230:441–454. [CrossRef]
[36] Sunil Kumar K, Kamalakar V, Palani S, Muniamuthu S, Belinda CM. Design of K-type propeller optimized with lightweight aluminum material and its CFD analysis for marine-based applications. In: Suresh P, Subbarayan S, Gunasekaran S, editors. Sustainable Communication Networks and Application. Lecture Notes in Networks and Systems, vol 1072. Singapore: Springer; 2024. p. 375–390. [CrossRef]
[37] Zhang Y, Ma S, Shao W, Zhang Y. Numerical investigation on the water entry of curved wedge-shaped sections into waves. Ocean Eng 2023;275:114155. [CrossRef]
[38] Huang Q, Wang C, Shi Y, Pan G, Liu G. Study of the cavity and hydrodynamic characteristics of water entry for projectiles with different wave parameters. Ocean Eng 2024;313:119441. [CrossRef]
[39] Wang K, Ma X, Bai W, Qian L, Li Z, Li Y. Two-dimensional numerical simulation of water entry of a cylinder into waves using OpenFOAM. Ocean Eng 2023;269:113516. [CrossRef]
[40] Cui J, Gu CJ, Chen X, Li MY, Masvaya B. Numerical study of wedge entry in still water and waves using smoothed particle hydrodynamics methods. Ocean Eng 2023;280:114776. [CrossRef]
[41] Sener MZ, Aksu E. The effects of head form on resistance performance and flow characteristics for a streamlined AUV hull design. Ocean Eng 2022;257:111630. [CrossRef]
[42] Myring DF. Theoretical study of body drag in subcritical axisymmetric flow. Aeronaut Q 1976;27:186–194. [CrossRef]
[43] Dean RG, Dalrymple RA. Water wave mechanics for engineers and scientists. Advanced Series on Ocean Engineering, vol 2. Singapore: World Scientific Publishing Company; 1991. [CrossRef]
[44] Hirt CW, Nichols BD. Volume of fluid (VOF) method for the dynamics of free boundaries. J Comput Phys 1981;39:201–225. [CrossRef]
[45] Zhao K, Liu PLF. On Stokes wave solutions. Proc R Soc A Math Phys Eng Sci 2022;478:20210732. [CrossRef]
[46] Hoekstra M. Code verification, solution verification and validation in RANS solvers. In: 28th Symposium on Naval Hydrodynamics; 2010 Sep 12–17; Pasadena, CA, USA. 2010.
[47] Eça L, Vaz G, Hoekstra M. A verification and validation exercise for the flow over a backward facing step. In: Proceedings of the 5th European Conference on Computational Fluid Dynamics (ECCOMAS CFD 2010); 2010 Jun 14–17; Lisbon, Portugal. 2010.